Stress and strain from striated pebbles. Theoretical analysis of striations on a rigid spherical body linked to a symmetrical tensor

Alfredo Taboada

GEO-TER SARL, Cap Alpha av Europe, 34830 Clapiers, France; and Laboratoire de Géologie Structurale, URA 1371, Université de Montpellier II, Sciences et Techniques du Languedoc Place E. Bataillon, 34095 Montpellier Cédex 5, France

Abstract—Striations on a pebble are interpreted as resulting from slip due to either a homogeneous stress state or a small homogeneous coaxial deformation in the matrix. In terms of stress, striations are assumed to be parallel to the applied shear stress. In terms of strain, striations are considered to be parallel to the relative tangential displacement between the pebble and adjacent matrix particles. Slip on the surface of a spherical rigid body enclosed in a deformable matrix (brittle or ductile) is theoretically analysed for different stress and strain regimes. The analysis predicts the topology of the resulting striations and singularity distribution on the sphere.

Both in terms of stress and strain, the tangential vector field on the sphere's surface derives from a potential function proportional to the magnitude of the normal vector field. Tangential and normal vectors represent either shear and normal stresses, or displacement components (in terms of strain). The plot of continuous curves parallel to striations (integral curves) and of equipotential curves on the sphere, allows simultaneously the magnitude and orientation of the tangential and normal vector fields to be visualized. Close to singular points, the integral curves correspond to power laws and the equipotentials correspond to conic sections.

This theoretical analysis allows graphical method for estimating the stress ratio $(\sigma_2 - \sigma_3)/(\sigma_1 - \sigma_3)$ from striated faults to be proposed, once the orientations of the principal stress directions are known (i.e. by means of other graphical methods).

INTRODUCTION

THIS work concerns the study of deformation observed in conglomerates from sedimentary basins, such as foreland belt molassic basins. It is focused on the analysis and interpretation of striated pebbles that are found in these conglomerates.

Conglomerate beds next to a fault often display an internal deformation that is linked to the kinematics of the fault. The intensity and style of deformation, vary as a function of the distance to the fault plane (Combes 1984): near the fault plane, pebbles are often intensely fractured (cut into sections). The fractures are often dynamically compatible with movement observed along the main fault plane (Eidelman & Reches 1992). Away from the fault plane, deformation in the conglomerate decreases rapidly and concentrates in the matrix and at the contact between the matrix and the pebbles. Displacement on the matrix–pebble interface is manifested by striations, which result from the relative movement of objects included in the matrix (e.g. quartz grains) that are positioned near the pebble.

This work concerns the analysis of striated pebbles when deformations are *small*. It is considered that pebbles behave as rigid objects. Use is made of the notion that the information available from striations over the surface of a pebble can be compared with a population of striated faults, slickolites and tension gashes covering all possible orientations (Combes 1984, Schrader 1991). Thus, the study of striated pebbles allows the characterization of the local and regional stress and strain states, as shown by several microtectonic studies carried out in deformed conglomerate beds (Estevez *et al.* 1976, Cam-

predon *et al.* 1977, Combes 1984, Casagrande Fioretti 1985, Petit *et al.* 1985, Schrader 1988, Séranne 1988, Ritz 1991). When clasts come from recent deposits, they represent particularly interesting tectonic objects for analysing active fault kinematics (Combes 1984, Ritz 1991).

In this paper a theoretical study of striated pebbles is performed by comparison with models of striations on a spherical body, for different stress and strain regimes (this simple case has the advantage that it is entirely treated analytically). For the sake of clarity, theoretical formulation is done independently from the analysis of the results. The results of this study can be used to analyse similar geological problems at much larger scale: i.e. the interpretation of late shear zones observed around a rigid intrusion surrounded by more deformable rocks that act as a 'matrix', and even the analysis of stretching lineations around an arcuate lithospheric slab subducted below a more deformable plate.

The analysis of striations on a spherical body has been approached in two complementary ways, each depending on the mechanical behaviour of the matrix.

Matrix showing brittle behaviour

The first approach that is proposed is inspired from the methods that exist in brittle tectonics. It consists of interpreting striations observed on the pebble's surface in terms of stress, by supposing that the matrix that surrounds the pebble is subjected to a homogeneous stress state defined by a stress tensor. Although this assumption is not entirely valid, it constitutes a good approximation when deformations are small (Combes
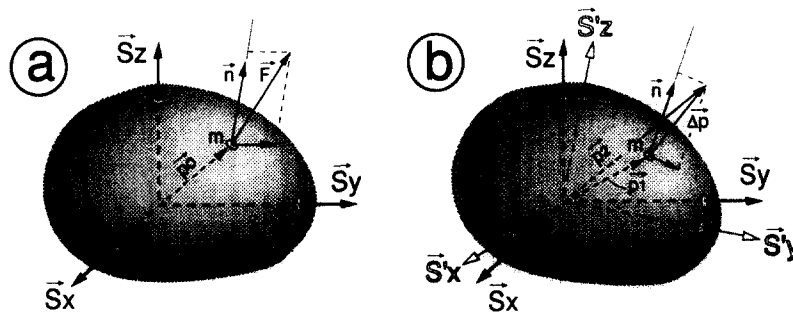
Fig. 1. Interpretation of the orientation of striations on the surface of a pebble, as a function of (a) stress regime and (b) strain regime.

1984, Casagrande Fioretti 1985, Séranne 1988, Ritz 1991).

A priori this approach can be applied to conglomerates whose matrix is well consolidated yet less resistant than clasts. In such cases the matrix often displays brittle behaviour and deformation is concentrated at the matrix–clast interface. Striations observed on the surface of the pebble can then be interpreted in terms of a simple mechanical model: the orientation of the striation at a point has the same direction as the applied shear stress in that point.

Supposing that the stress tensor is constant around the pebble, the applied stress at a point m of the pebble surface can easily be calculated (Fig. 1a):

Let n be the unit vector perpendicular to the pebble surface at m, and pointing outwards, defined with respect to an orthonormal reference frame $S = (S_x, S_y, S_z)$. The applied stress F at m is defined by $F = T n$, where T is a symmetrical 3×3 matrix representing the stress tensor in reference frame S.

This mechanical model is commonly used in brittle tectonics to interpret sliding along faults (Anderson 1951, Wallace 1951, Bott 1959, Carey & Brunier 1974), and to calculate parameters of the stress tensor from striated faults by means of inverse methods (i.e. Armijo & Cisternas 1978, Angelier 1979, 1990, Carey 1979, Etchecopar et al. 1981, Gephart & Forsyth 1984, Michael 1984, Reches 1987, Sassi & Carey-Gailhardis 1987, Galindo-Zaldivar & Gonzalez-Lodeiro 1988, Rivera & Cisternas 1990, Fleischmann & Nemcok 1991, Will & Powell 1991). Using this model, many authors have calculated parameters of the stress tensor at the outcrop scale, from slip data measured in conglomerates. Some of them have calculated the orientation of the principal compressive axis from penetrative striations (slickolites) measured on the pebble surface (Estevez et al. 1976, Campredon et al. 1977). Others have treated the surface of striated pebbles as microfaults, and they have calculated the orientation of the stress principal axes and the shape ratio of the stress ellipsoid (Combes 1984, Casagrande Fioretti 1985, Séranne & Séguret 1987, Ritz 1991).

These previous studies have been made on conglomerates from both shallow and deeper structural levels containing clasts of varying lithologies and sizes, and clayey–sandy matrices moderately to well cemented.

Matrix showing ductile behaviour

The second approach consists of interpreting the striations on pebbles as a function of the strain of the matrix surrounding the pebble and of the rotation of the pebble. A priori this approach can be applied to conglomerates whose matrix behaviour is ductile.

The following definitions are necessary.

Let $S = (S_x, S_y, S_z)$ and $S' = (S'_x, S'_y, S'_z)$ be two orthonormal reference frames whose origin coincides with the centre of gravity of the pebble. It is supposed that the orientation of S is fixed with respect to the geographic reference frame and S' is fixed with respect to the pebble, the two systems being parallel before deformation. Thus, the orientation of S' can change if the pebble rotates during deformation (Fig. 1b).

The assumption is made that the average deformation in the conglomerate is homogeneous. Again, this assumption is justified for small deformations (Schrader 1988). However, at smaller scales strain is heterogeneous because of the rheological contrast between the clasts and the matrix: i.e. away from the clast matrix, the strain is approximately homogeneous, and close to the clast matrix particles are restricted to move tangentially to its surface. The average deformation in the conglomerate layer is characterised in reference frame S by a transformation matrix L whose determinant is positive (Germain 1986). An orthonormal matrix R and two symmetrical positively defined matrices V and W can be associated with L, such that $L = RV = WR$. R represents the rotational component of L, and V and W the pure deformation components before or after rotation, respectively (Germain 1986).

Let Ω be the transformation matrix between systems S' and S after deformation. Thus Ω is orthogonal and it characterizes the rigid rotation of the pebble. Let m be a material point of the pebble surface and p_0 the vector indicating the initial position of m in S (Fig. 1a). After deformation, point m will move to a new position $p_1 = \Omega p_0$ in system S (Fig. 1b). If the matrix and the pebble had the same competence, the small-scale strain pattern would be homogeneous and the particles of the matrix that are in contact with point m at the initial state, would move to point $p_2 = L p_0$ in S. Let $\Delta p = p_2 - p_1 = (L - \Omega) p_0$ be the displacement vector between the two points defined previously (Fig. 1b). It is supposed that the orientation of the striation at m has the same direction as
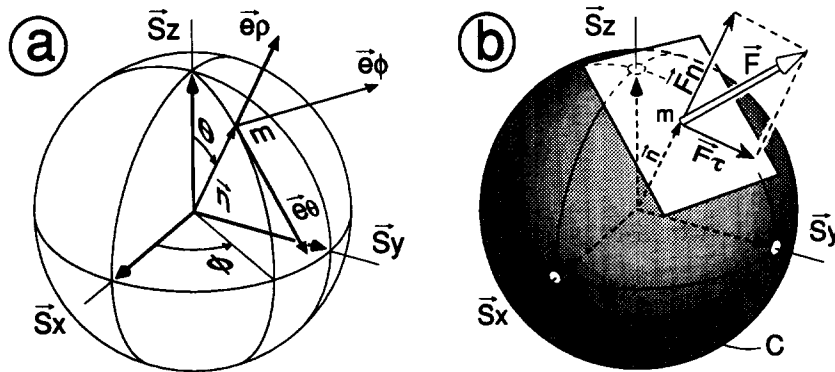
Fig. 2. (a) Spherical co-ordinates reference frame used to locate the position of points on the surface of the unitary sphere (modified from Spiegel 1987). (eΘ, eϕ, eρ) = local orthonormal reference frame. (b) Decomposition of vector F associated with a point m on the surface of the sphere, in a normal component $\mathbf{F}_n$ and a tangential component $\mathbf{F}_\tau$.

the projection of $\Delta\mathbf{p}$ on the surface of the pebble. $\Delta\mathbf{p}$ can be expressed as a function of the co-ordinates of point m in S in the final state:

$$\Delta\mathbf{p} = (L - \Omega)\Omega^T \mathbf{p}_1 = D\,\mathbf{p}_1, \tag{1}$$

where the operator D defines the displacement tensor (De Paor 1983) between the pebble at the final state and the matrix that surrounds it.

Several models can be considered to evaluate the differential rotation of the pebble in the matrix. Etchecopar & Malavieille (1987) have proposed that the rotation of a rigid object in a more deformable matrix is such that gaps and boundary sliding are minimized. The rotation of the object, associated with an incremental deformation in the matrix is defined by the minimization of a function. This function depends on the sum of the squares of the distance between the object and the matrix, for regularly spaced points located at the surface of the rigid object. It can be supposed that the rotation of a *spherical pebble* included in a homogeneous ductile matrix that undergoes a non-coaxial deformation regime, is characterized by matrix R which is the rotational component of transformation matrix L. Consequently

$$D = (L - R)R^T = W - I. \tag{2}$$

The particular case in which the pebble does not rotate is quite interesting because striations can be directly interpreted in terms of matrix L (i.e. $D = L - I$). This case can occur when the deformation history is coaxial, if the pebble is symmetric and if its symmetry axes are parallel to the principal strain axes. The existence of other pebbles in the matrix can also limit the rotation of the pebble independently of the deformation regime.

THEORETICAL ANALYSIS OF STRIATIONS ON A SPHERICAL PEBBLE

For the two situations set forth above, the striation field on a spherical pebble will now be calculated for different stress and displacement tensors. In the interpretation in terms of stress, the orientation of the

striation at a point m of the pebble surface depends on the orientation of the vector normal to the surface at m; in the interpretation in terms of strain, it depends on the co-ordinates of point m with respect to a reference frame whose origin is located on the centre of gravity of the pebble. The surface of the sphere is particularly interesting, because the normal vector at point m is parallel to the vector indicating the position of m with respect to the centre of the sphere. A direct consequence of this property is that striation fields associated with identical stress or displacement tensors are equal. Knowing that the stress tensor is symmetrical by definition, the analogy between striation fields can only be drawn if matrix D that was previously defined, is also symmetric. A particular case that satisfies this condition is the coaxial deformation history, where it is supposed that for a spherical pebble $\Omega = I$ (identity matrix, no rotation). The analogy between striation fields is only valid for the surface of the sphere. *For any other geometrical form, the striation fields deduced from the two hypotheses are different.* However, this simple case assists our understanding striation patterns on natural examples. The problem concerning the striation field on the surface of the sphere, associated with a stress tensor or a displacement tensor in coaxial strain regime is treated analytically.

Striations associated with a symmetrical tensor

Formulation of the model. Let T be a symmetric tensor in its principal reference frame S. T represents a stress tensor as well as a displacement tensor in a coaxial strain regime such that the pebble does not rotate. T can be expressed by means of a diagonal matrix:

$$T = \begin{bmatrix} \lambda_x & 0 & 0 \\ 0 & \lambda_y & 0 \\ 0 & 0 & \lambda_z \end{bmatrix}, \tag{3}$$

where λ_x, λ_y and λ_z are the eigenvalues of the tensor in the directions S_x, S_y and S_z, respectively. Let C be the surface of the unit sphere centred with respect to S, and let m be a point in this surface (Fig. 2). Vector n indicates the position of m in S, and represents the unit vector perpendicular to C at m. n can be defined in spherical co-

ordinates by means of angles ϕ and Θ, which represent the azimuth of n and its inclination with respect to the vertical axis, respectively (Fig. 2a):

$$\mathbf{n} = \begin{bmatrix} \sin(\Theta)\cos(\phi) \\ \sin(\Theta)\sin(\phi) \\ \cos(\Theta) \end{bmatrix}. \tag{4}$$

A vector F can be associated with each point m in C:

$$\mathbf{F} = T\mathbf{n} = \begin{bmatrix} \lambda_x \sin(\Theta)\cos(\phi) \\ \lambda_y \sin(\Theta)\sin(\phi) \\ \lambda_z \cos(\Theta) \end{bmatrix}. \tag{5}$$

F represents either the applied stress on m, or the displacement of particles adjacent to point m, depending on the considered interpretation (Fig. 2b). F can be decomposed into a component $\mathbf{F_n}$, which is normal to the surface of the sphere, and a tangential component $\mathbf{F_r}$, such that $\mathbf{F} = \mathbf{F_n} + \mathbf{F_r}$. The magnitudes of vectors $\mathbf{F_n}$ and $\mathbf{F_r}$ are F_n and F_r, respectively. Let (eΘ,eϕ,eρ) be the local orthonormal reference frame in spherical coordinates, defined in terms of Θ and ϕ (Fig. 2a):

$$\mathbf{e\Theta} = \begin{bmatrix} \cos(\Theta)\cos(\phi) \\ \cos(\Theta)\sin(\phi) \\ -\sin(\Theta) \end{bmatrix},$$

$$\mathbf{e\phi} = \begin{bmatrix} -\sin(\phi) \\ \cos(\phi) \\ 0 \end{bmatrix},$$

$$\mathbf{e\rho} = \begin{bmatrix} \sin(\Theta)\cos(\phi) \\ \sin(\Theta)\sin(\phi) \\ \cos(\Theta) \end{bmatrix}. \tag{6}$$

The transformation matrix between systems ($\mathbf{S_x}$, $\mathbf{S_y}$, $\mathbf{S_z}$) and (eΘ,eϕ,eρ) is defined by:

$$M = \begin{bmatrix} \cos(\Theta)\cos(\phi) & \cos(\Theta)\sin(\phi) & -\sin(\Theta) \\ -\sin(\phi) & \cos(\phi) & 0 \\ \sin(\Theta)\cos(\phi) & \sin(\Theta)\sin(\phi) & \cos(\Theta) \end{bmatrix}. \tag{7}$$

Notice that the lines of this matrix correspond to vectors eΘ, eϕ and eρ.

Vector F can be expressed in system (eΘ, eϕ, eρ), making use of transformation matrix M:

$$\mathbf{F'} = M\mathbf{F}$$

$$= \begin{bmatrix} \sin(\Theta)\cos(\Theta)(\lambda_x \cos^2(\phi) + \lambda_y \sin^2(\phi) - \lambda_z) \\ (\lambda_y - \lambda_x)\sin(\Theta)\cos(\phi)\sin(\phi) \\ (\lambda_x \cos^2(\phi) + \lambda_y \sin^2(\phi))\sin^2(\Theta) + \lambda_z \cos^2(\Theta) \end{bmatrix}$$

$$= \begin{bmatrix} F'_{e\Theta} \\ F'_{e\phi} \\ F'_{e\rho} \end{bmatrix}, \tag{8}$$

where $F'_{e\Theta}$ is the component of $\mathbf{F_r}$ in the dip direction, $F'_{e\phi}$ is the component of $\mathbf{F_r}$ in the azimuth direction and $F'_{e\rho}$ is equal to $\mathbf{F_n}$ (Fig. 3). The set of vectors $\mathbf{F_r}$ defines a vector space, tangent to the sphere (for the definition of tangent vector space see Arnold 1988, Chap. 5, Munkres 1991, Chap. 6). The orientation of vector $\mathbf{F_r}$ on the plane
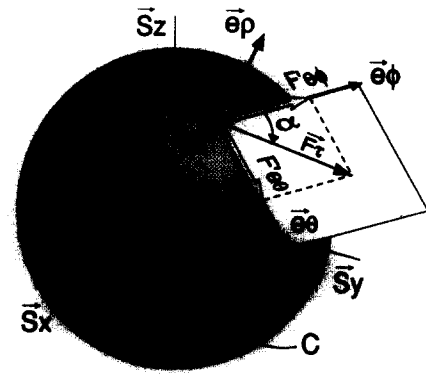

Fig. 3. Components of vector F in co-ordinate system (eΘ, eϕ, eρ).

that is tangent to the sphere at m, can be calculated by noting that:

$$\tan(\alpha) = \frac{F'_{e\Theta}}{F'_{e\phi}}$$

$$= \cos(\Theta)\left[\frac{R_x}{\cos(\phi)\sin(\phi)} - \frac{\cos(\phi)}{\sin(\phi)}\right]$$

$$= v(\Theta, \phi), \tag{9}$$

such that

$$R_x = \frac{(\lambda_y - \lambda_z)}{(\lambda_y - \lambda_x)},$$

where a is the clockwise angle between eϕ and vector $\mathbf{F_r}$ (Fig. 3). The previous equation shows that the orientation of $\mathbf{F_r}$ in a point m of the unit sphere depends on the orientation of unit vector n and on R_x, which defines a ratio between the tensor deviators. This result is consistent with the Bott principle (1959), which states that the orientation of the striation on a fault plane depends on the orientation of the stress principal axes and on a ratio that characterizes the form of the stress ellipsoid.

A direction field $\bar{\omega}$ is defined on the surface of the sphere, by associating to each one of its points a straight line that is parallel to $\mathbf{F_r}$. By definition, these lines are tangent to the sphere and their directing coefficient in the plane (eϕ,eΘ) is given by $v(\Theta,\phi)$. The integral curves of the direction field $\bar{\omega}$ on the surface of the sphere will be calculated. By definition $\mathbf{F_r}$ is tangent to integral curves in every point of the sphere (Fig. 4a) (for the definition of integral curve see Arnold 1988, Chap. 1, pp. 14–17).

The differential of distance in spherical co-ordinates is defined by (Fig. 4b):

$$ds = d\rho\,\mathbf{e\rho} + \rho\,d\Theta\,\mathbf{e\Theta} + \rho\sin(\Theta)\,d\phi\,\mathbf{e\phi} \Rightarrow$$

$$\tan(\alpha) = \frac{\rho\,d\Theta}{\rho\sin(\Theta)\,d\phi}$$

$$= \cos(\Theta)\left[\frac{R_x}{\cos(\phi)\sin(\phi)} - \frac{\cos(\phi)}{\sin(\phi)}\right]. \tag{10}$$

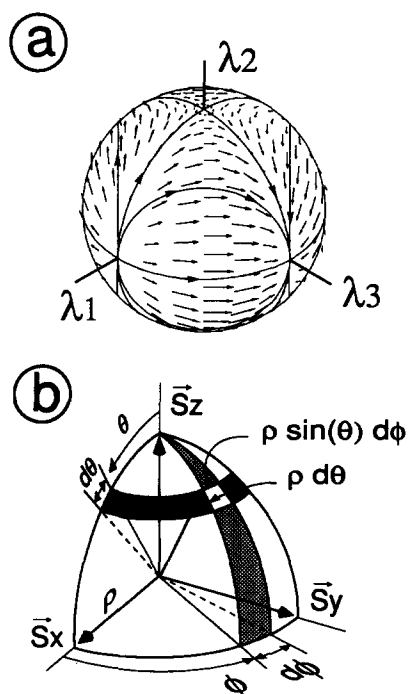This differential equation can be solved by separating variables Θ and ϕ and integrating:

Fig. 4. (a) Example of vector field (F_r), tangent to the surface of the sphere, such that $\lambda_1 < \lambda_3$ and $\lambda_2 = (\lambda_1 + \lambda_3)/2$. Continuous curves are parallel to the orientation of vector F_r in every point of the sphere. These curves are called *integral curves*. (b) Lengths of arc differentials in spherical co-ordinates (modified from Spiegel 1987).

$$\int \frac{d\Theta}{\cos(\Theta)\sin(\Theta)} = \int \left[\frac{R_x}{\cos(\phi)\sin(\phi)} - \frac{\cos(\phi)}{\sin(\phi)}\right] d\phi. \quad (11)$$

This integral is evaluated in Appendix A, and the resulting equation that defines the integral curves is given by:

$$\tan(\Theta = \pm k_1 |\sin(\phi)|^{R_x-1}|\cos(\phi)|^{-R_x}$$

$$= \pm k_1 |\sin(\phi)|^{(\lambda_x-\lambda_z)/(\lambda_y-\lambda_x)}|\cos(\phi)|^{(\lambda_z-\lambda_y)/(\lambda_y-\lambda_x)},$$

$$k_1 > 0, \phi \neq n\pi/2, \quad (12)$$

where k_1 is a constant of integration.

Analysis of integral curves for different symmetric tensors

Many authors have studied slickenline patterns on the surface of the sphere linked to symmetrical and non-symmetrical tensors (i.e. Wallace 1951, Hoeppener *et al.* 1983, Aleksandrowski 1985, Schader 1988, Twiss *et al.* 1991). However, analytical equations for integral curves have not been calculated. Thus, in this section integral curves are derived corresponding to the different stress and coaxial deformation states that can be found in the upper crust, according to a schematic classification which only considers four parameters: a ratio that defines the form of the ellipsoid associated with T, and the orientation of the three eigenvectors in space (i.e. the principal axes of the tensor) (Anderson 1951, Philip 1987, Guiraud *et al.* 1989, Ritz 1991). This analysis will prove to be compatible with results of previous studies and it will serve to introduce the remaining sections.

Definitions. (a) Let λ_1, λ_2 and λ_3 be the eigenvalues of T, such that $\lambda_1 \leq \lambda_2 \leq \lambda_3$, and let v_1, v_2 and v_3 be the corresponding eigenvectors.

(b) Let S_1, S_2 and S_3 be unit vectors parallel to v_1, v_2 and v_3, respectively.

(c) Let $R = (\lambda_2 - \lambda_3)/(\lambda_1 - \lambda_3)$ be the parameter characterizing the shape ratio of the ellipsoid associated with T.

In terms of stress, λ_1, λ_2 and λ_3 represent the magnitudes of the compressive, intermediate and tension axes $(\sigma_1, \sigma_2, \sigma_3)$, respectively. In terms of strain, λ_1, λ_2 and λ_3 represent the elongations of the lesser, intermediate and greater principal axes $(\varepsilon_1, \varepsilon_2, \varepsilon_3)$.

Three different regimes are examined:

(a) The regime where S_1 is vertical (normal or extensive regime).

(b) The regime where S_2 is vertical (strike-slip).

(c) The regime where S_3 is vertical (thrust or compressive).

For each regime five different tensors are considered whose shape ratios vary between two limit values: $R = 0$ and $R = 1$. When $R = 0$, the eigenvalues λ_2 and λ_3 are equal; when $R = 1$, the eigenvalues λ_2 and λ_1 are equal. Stress and strain ellipsoids in space corresponding to the schematic classification are illustrated in Fig. 5. In the case of strain, the ellipsoids represent the final state of a spherical surface submitted to a homogeneous strain $L = T + I$. All the eigenvalues of the operator L are positive. Notice that for the same tensor T, the associated stress and strain ellipsoids are different. This results from having considered negative eigenvalues in the case of stress ellipsoids, since in general stresses in the upper crust are compressive (negative). Applied stress vectors are to be interpreted from the ellipsoid as vectors directed towards its centre.

To describe integral curves in the different cases, the following definitions are used (Fig. 6).

(a) Let p_1, p_2 and p_3 be the points on the surface of the unit sphere, corresponding to vectors S_1, S_2 and S_3.

(b) Planes whose perpendicular is an eigenvector are called principal planes. A principal plane is defined by two non-parallel vectors that lie in the plane: χ_{ij} is the principal plane containing S_i and S_j.

(c) The intersection between the surface of the unit sphere and a principal plane χ_{ij}, defines a principal circle κ_{ij} on the sphere.

Figure 7(a) illustrates integral curves on the surface of the sphere for different tensors in extensive (NR), strike-slip (SS) and compressive (RR) regimes. These curves are oriented in the same direction as F_r. Figure 7(b) illustrates the projection of these curves in a normalized Mohr diagram, where the abscissa axis represents F_n and the ordinate axis represents F_r. In terms of stress, a point (F_n, F_r) in the Mohr diagram indicates the magnitudes of the applied normal and shear stresses in a point of the sphere. In terms of strain, the couple (F_n, F_r) represents the displacements of a point, perpendicularly and tangentially to the surface of the sphere (De Paor 1983). In all cases the integral curves on the sphere are symmetrical with respect to the principal
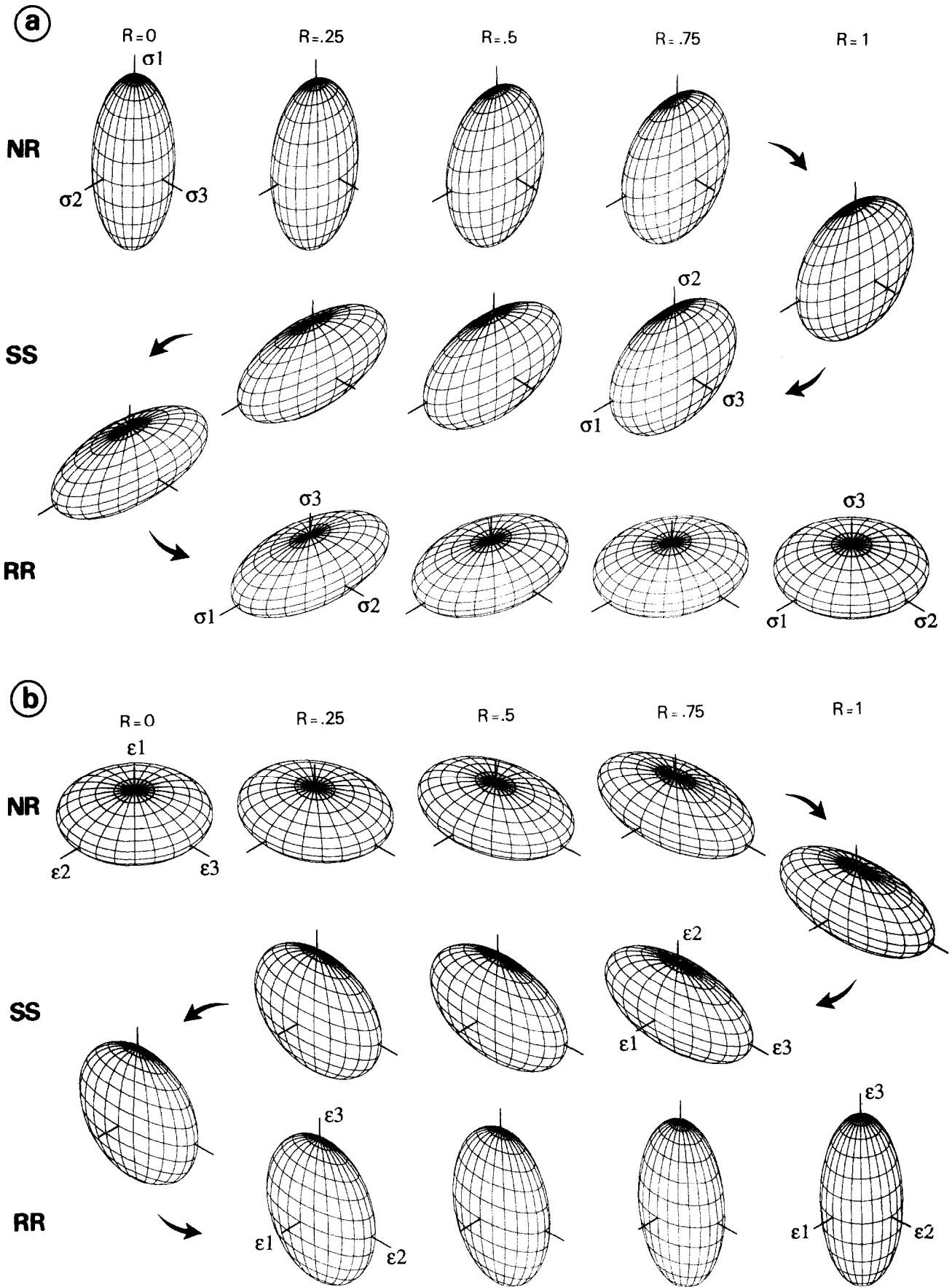
Fig. 5. Representation of (a) stress and (b) strain ellipsoids, for different tectonic regimes. NR = normal regime; SS = strike-slip regime; RR = reverse regime; σ_1, σ_2 and σ_3 indicate the compressive, intermediate and extensive principal stress axes; ε_1, ε_2 and ε_3 indicate the minor, intermediate and major principal axes in terms of strain. Deformed 'latitude' and 'longitude' lines were regularly spaced on the sphere before deformation. $R = (\lambda_2 - \lambda_3)/(\lambda_1 - \lambda_3)$ defines the ellipsoid's shape ratio.
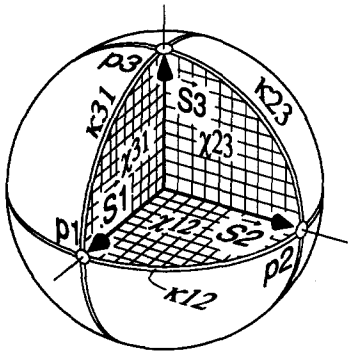
Fig. 6. Localization of points p_i, principal planes χ_{ij} and principal circles κ_{ij} on the surface of the sphere, as a function of the orientation of vectors $S_i(i, j = 1, \ldots, 3)$.

p_1, go round p_2 and converge towards p_3 (Figs. 6 and 7a). In addition, they tend to become parallel to principal circles κ_{12} and κ_{23}. Points p_1, p_2 and p_3 are singular points where F_τ is zero, and thus the orientation of the striation is not defined. Strictly speaking, p_1 corresponds to a diverging node, p_2 to a saddle point and p_3 to a converging node.

—When $R = 0$, the integral curves are parallel to great circles whose axis of revolution is S_1 (Fig. 7a). The curves diverge from p_1, and converge steadily towards principal circle κ_{23} (dashed curve in Fig. 7a) where F_τ is zero. Notice that in this case, curves are unstable with respect to variations of the shape ratio R close to principal circle κ_{23}: they are subperpendicular to κ_{23} when $R = 0$, and subparallel to κ_{23} when $R > 0$.

—When $R = 1$, the integral curves are parallel to great circles whose axis of revolution is S_3 (Fig. 7a). Curves diverge from principal circle κ_{12} (dashed curve in Fig. 7a). where F_τ is zero, and converge steadily towards p_3. In this case, the curves are unstable with respect to variations of the shape ratio R close to principal circle

planes. Moreover, for a fixed R ratio the curves corresponding to the three regimes are equivalent if the sphere is rotated such that the principal directions S_1, S_2 and S_3 are parallel. The disposition of curves varies depending on the value of the ellipsoid shape ratio R.

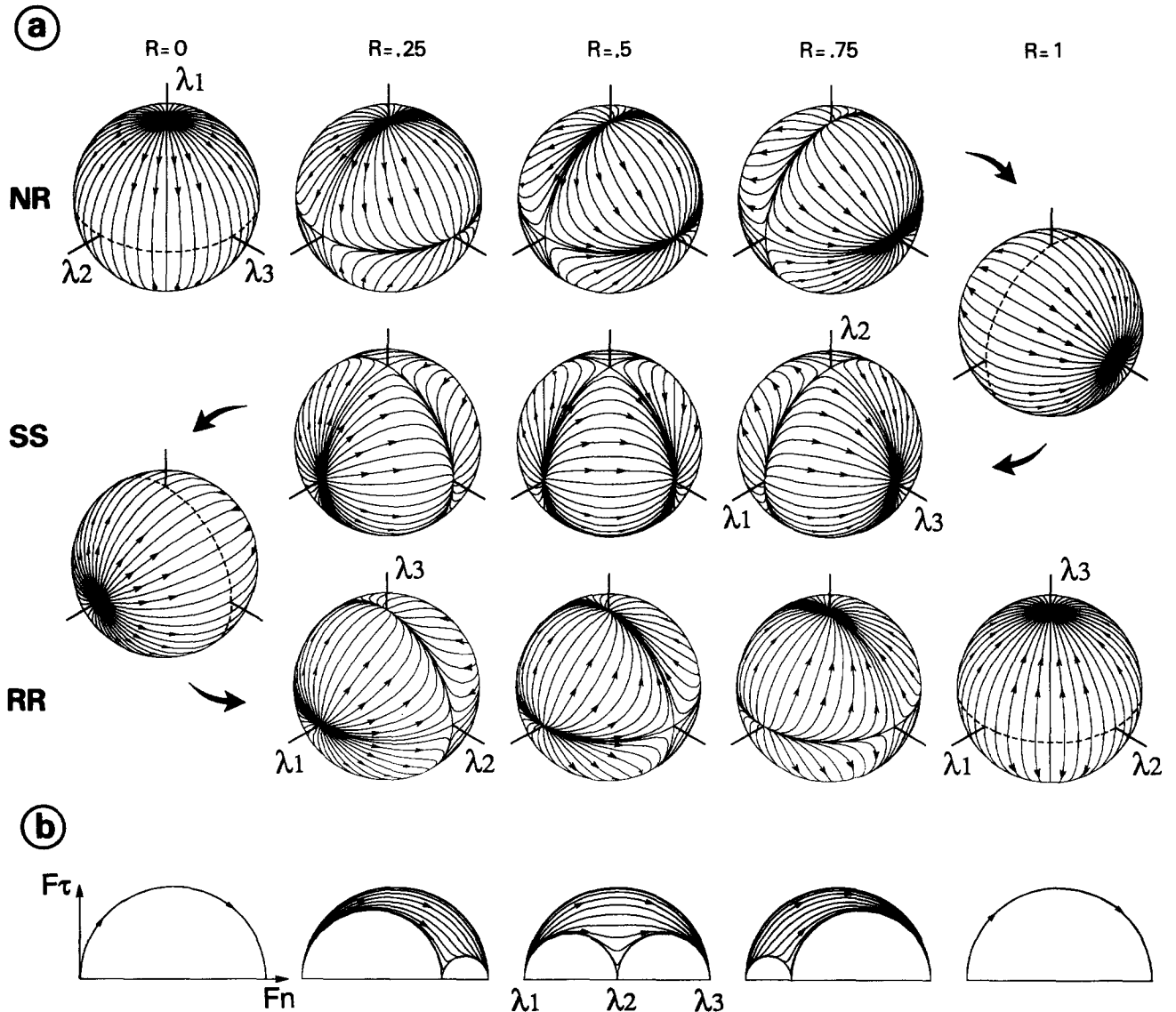—When $R \neq 0$ and $R \neq 1$, integral curves diverge from

Fig. 7. Integral curves on the surface of the sphere (a) and in the Mohr diagram (b) for different tectonic regimes. These curves are parallel to vector F_τ at every point on the sphere. Same conventions as in Fig. 5. Dashed lines indicate principal circles where $F_\tau = 0$. Explanations in the text.

κ_{12}: they are subperpendicular to κ_{12} when $R = 1$, and subparallel to κ_{12} when $R < 1$.

Apart from the particular cases above, the disposition of curves changes progressively for different values of the R ratio. Close to the principal circle κ_{13} curves are subparallel to κ_{13} for all values of the R ratio.

Wallace (1951) plotted curves that are analogous to the integral curves that have been calculated analytically: he represented on a stereographic projection curves that are parallel to the shear stress in every point, for several stress tensors in extensive regime. Some of the observations by Schrader (1988) on the orientation of striations on quasi-spherical pebbles are very consistent with the general disposition of the calculated integral curves. In particular, those where the three axes of the lineation field are perpendicular to each other (orthorombic field).

Notice that integral curves in the Mohr diagram vary between two limiting curves (Fig. 7b): the curve passing by κ_{13}, which corresponds to principal circle (λ_1, λ_3), and the curve passing by κ_{12} and κ_{23}, which corresponds to circles (λ_1, λ_2) and (λ_2, λ_3). The passage between these two curves is progressive.

Potential function

The set of vectors $\mathbf{F}_\tau$ associated with tensor T, defines a vector field tangent to the surface of the sphere, and the magnitude of $\mathbf{F}_n$ defines a scalar field on this surface. It will be proved that in every point of this surface:

$$\mathbf{F}_\tau = \tfrac{1}{2} \nabla_S |\mathbf{F}_n|, \tag{13}$$

where ∇_S is the gradient operator limited to the surface of the sphere. This equation states that the tangential component of $\mathbf{F}$ on the surface of the sphere ($\mathbf{F}_\tau$), is the gradient of a potential function that is proportional to the magnitude of the normal component of $\mathbf{F}$ (F_n). Thus, vector field $\mathbf{F}_\tau$ on the surface of the sphere is conservative. The magnitude and direction of $\nabla_S |\mathbf{F}_n|$ in a point, are those of the algebraically maximum directional derivative of F_n on the plane tangent to the surface of the sphere. Thus, vector $\mathbf{F}_\tau$ is proportional to the maximum directional derivative of F_n on the surface of the sphere. Equation (13) can be proved directly by evaluating the gradient on the surface of the sphere, of the potential function $[(1/2) |F_n|]$ (see Appendix B).

According to this equation, $\mathbf{F}_\tau$ is perpendicular at every point to the curves where F_n is constant. Thus, integral curves that are parallel to $\mathbf{F}_\tau$ in every point are also perpendicular to the curves of equal value of F_n (iso-F_n). This fact was observed by Wallace (1951), who noticed that iso-normal stress curves were perpendicular to the shear stress vector in every point of an angle-preserving stereographic projection. Vector $\mathbf{F}$ can be defined in any point of the surface of the sphere by means of the following equation:

$$\mathbf{F} = F_n \, \mathbf{e\rho} + \tfrac{1}{2} \nabla_S |\mathbf{F}_n|. \tag{14}$$

Using the previous equations, iso-F_n and integral curves have been plotted for the different tensors of the

schematic classification set forth previously (Fig. 8a). These curves have also been projected on the Mohr diagram representation (Fig. 8b). The iso-F_n curves will be called equipotentials since the value of the potential function is constant along each one of them.

The disposition of the equipotentials on the sphere can be used to estimate the magnitude of $\mathbf{F}_\tau$ in any point. Let A and B be two points belonging to an integral curve Γ, then the line integral of $\mathbf{F}_\tau$ along Γ is equal to the potential difference between A and B:

$$\int_\Gamma \mathbf{F}_\tau \cdot d\gamma = \int_A^B \mathbf{F}_\tau \cdot d\gamma = \tfrac{1}{2}(F_{n_B} - F_{n_A}) = \tfrac{1}{2} \Delta F_n, \tag{15}$$

where $d\gamma$ is a vector whose magnitude is equal to the differential of arc of curve Γ, which is parallel to $\mathbf{F}_\tau$. This integral can be interpreted as the flow of vector $\mathbf{F}_\tau$ along Γ between A and B. Knowing that vector field $\mathbf{F}_\tau$ is conservative, the value of the integral is independent of the integration path between points A and B. If $\mathbf{F}_\tau$ is interpreted in terms of stress, the previous integral represents the work done by the shear stress between points A and B, and function $[(1/2)F_n]$ represents the associated potential energy. If A and B belong to two contiguous equipotentials, then:

$$\int_A^B \mathbf{F}_\tau \cdot d\gamma = F_{\tau_m}\gamma = \tfrac{1}{2} \Delta F_n, \tag{16}$$

where F_{τ_m} is the mean value of $\mathbf{F}_\tau$ in the interval, and γ is the length of the interval. The potential difference being constant between two contiguous equipotentials, F_{τ_m} is inversely proportional to the length of the interval. Thus, F_{τ_m} is high in zones where contiguous equipotentials are close to each other. Conversely, F_{τ_m} is low in zones where the distance between two contiguous equipotentials is large. In Fig. 8(a) the zones where F_τ is the lowest are located close to points p_1, p_2 and p_3 (Fig. 6). F_τ is zero in these three points and thus F_n remains quite constant around these points. Notice that the zone where F_τ is high changes with respect to the shape ratio of the ellipsoid.

—For R ratios close to 0, this zone corresponds to a band of revolution about S_1.

—For R ratios close to 1, it corresponds to a band of revolution about S_3.

The most negative value (compressive in terms of stress) of F_n is reached in point p_1, because integral curves diverge from this point. Thus, F_n increases when moving away from p_1, where its value is λ_1. In the same way, the most positive value of F_n is defined in point p_3 ($F_n = \lambda_3$) since integral curves converge towards this point. Thus, F_n decreases when moving away from this point. When following an integral curve between p_1 and p_3, F_n is defined by an increasing function such that $F_n \in (\lambda_1, \lambda_3)$. In Fig. 8 the equipotential corresponding to $F_n = \lambda_2$ is defined by a great circle through S_2. The orientation of this great circle can be calculated as a function of the ellipsoid shape ratio R in a strike-slip regime, with

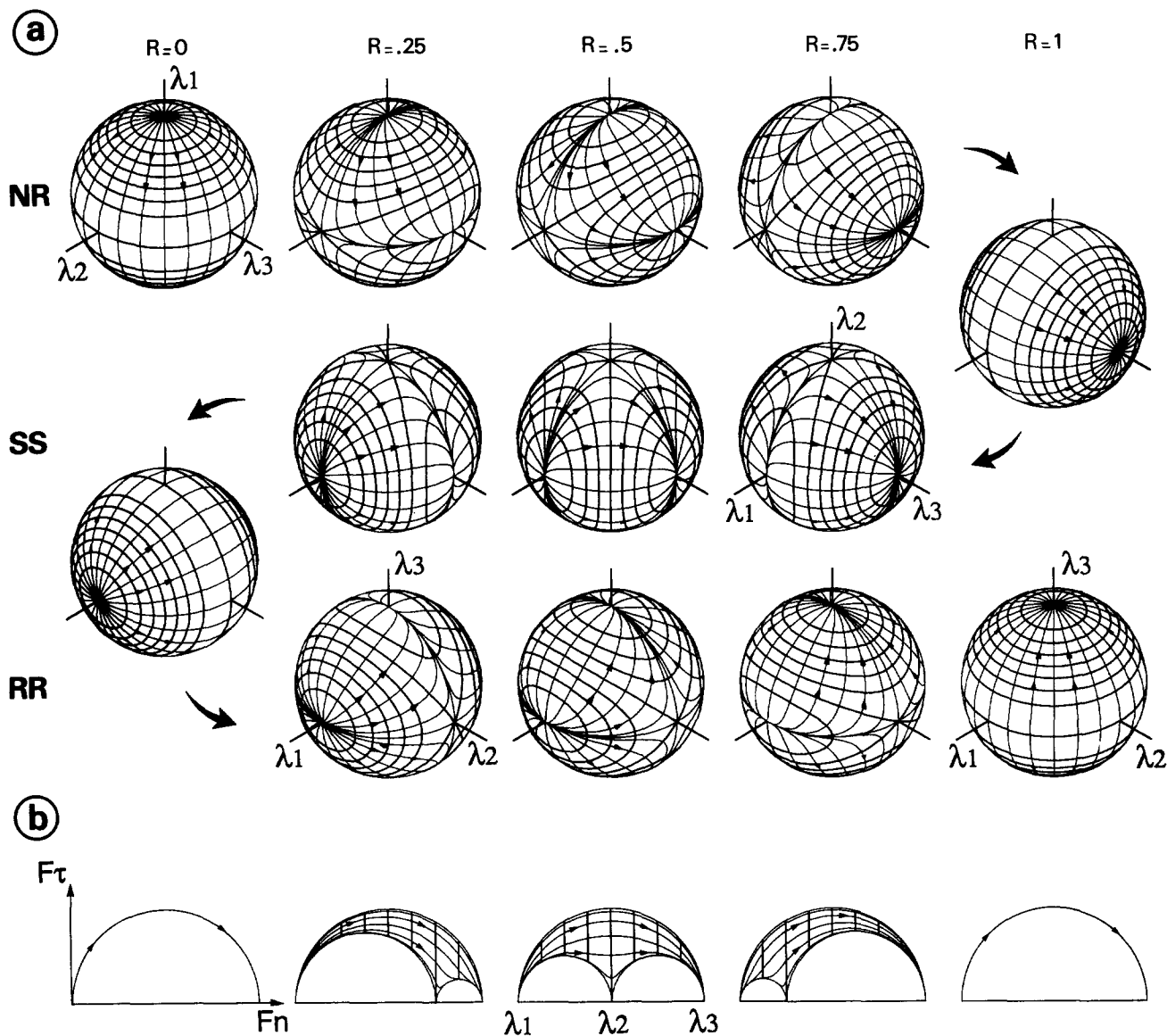$$\lambda_x = \lambda_1, \quad \lambda_y = \lambda_3 \quad \text{and} \quad \lambda_z = \lambda_2.$$

Fig. 8. Iso-F_n curves (i.e. vertical lines in Mohr diagram) and integral curves on the surface of the sphere (a) and in the Mohr diagram (b) for different tectonic regimes. Notice that these two families of curves are perpendicular to each other on the surface of the sphere. Same conventions as in Fig. 5. Explanations in the text.

For these values in equation (8) and if $F_n = \lambda_2$, then:

$$(\lambda_1 \cos^2(\phi) + \lambda_3 \sin^2(\phi)) \sin^2(\Theta) + \lambda_2 \cos^2(\Theta) = \lambda_2$$

$$\Rightarrow \lambda_2 = \lambda_1 \cos^2(\phi) + \lambda_3 \sin^2(\phi)$$

$$= (\lambda_1 - \lambda_3) \cos^2(\phi) + \lambda_3$$

$$\Rightarrow R = \frac{(\lambda_2 - \lambda_3)}{(\lambda_1 - \lambda_3)} = \cos^2(\phi). \tag{17}$$

This equation permits the calculation of the azimuth with respect to S_1, of the great circle where $F_n = \lambda_2$ in a strike-slip regime. This great circle is particularly interesting because integral curves intersect it perpendicularly. Thus, the orientation of $\mathbf{F}_\tau$ in space is constant for all the planes that are tangent to the sphere along this great circle, independently of the orientation of the tensor. This property is in agreement with results by Vergely *et al.* (1987), who plotted on a stereonet curves indicating the orientation in space of the theoretical

striation for planes whose azimuth or dip varies, the other parameter remaining constant. For a given stress regime, they noticed that the different curves intersected in two points (focus) situated in the plane (σ_1, σ_3). These two points indicate the orientation of the theoretical striation for fault planes of variable orientation that share a common line (the striation). These authors propose a formula equivalent to equation (17). In a strike-slip regime, the great circle where $F_n = \lambda_2$ is such that $\mathbf{F}_\tau$ is horizontal, because integral curves are perpendicular to it (Fig. 8a). This great circle separates a domain where the direction of $\mathbf{F}_\tau$ is strike-slip reverse, from a domain where it is strike-slip normal. These domains correspond to two well defined zones in the Mohr diagram representation:

—strike-slip reverse domain if $F_n \in (\lambda_1, \lambda_2)$;
—strike-slip normal domain if $F_n \in (\lambda_2, \lambda_3)$.

These domains vary as a function of the R ratio: if R is close to 0, the great circle will be close to κ_{23} and the strike-slip reverse domain will be larger; conversely, if R
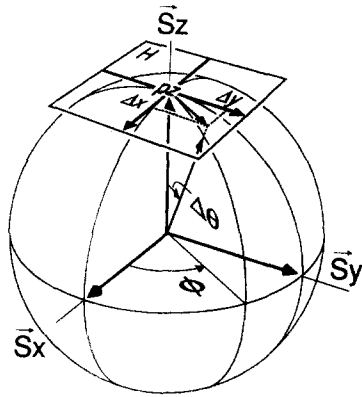
Fig. 9. Representation of the horizontal plane H, tangent to the sphere in point p_z. $(\Delta x, \Delta y)$ = Cartesian co-ordinates of a point on the sphere, localized near singular point p_z.

is close to 1, the great circle will be close to κ_{12} and the strike-slip normal domain will prevail.

These results are consistent with the analysis on fault reactivation by Tajima & Célérier (1989) who proposed a diagram in which the type of faulting (normal, reverse and strike-slip) is related to a ratio between stress deviators and to fault plane azimuth. The limit between normal and reverse faulting components in strike-slip stress regime is given by an analogous equation.

Analysis of singular points

Observations on deformed conglomerates by several authors confirm the existence of singular points on the surface of striated pebbles. Dissolution poles from where striations diverge were described by Estevez *et al.* (1976) and Campredon *et al.* (1977). Combes (1984) observed non-striated 'neutral bands' on the faces of the pebbles that are perfectly parallel to the shortening direction. These 'neutral bands' clearly correspond to the principal circle κ_{23} on the surface of the sphere, for a revolution ellipsoid about S_1 (Fig. 7). Casagrande Fioretti (1985) pointed out analogous observations in a stress regime close to radial compression, where he observed horizontal stylolitic bands. Finally, Schrader (1988) established the correlation between the location of singular points and different strain paths.

Since these singular points are clearly identifiable in the field, it is worth understanding their significance. Thus, analytical expressions will be calculated to describe integral curves and equipotentials near singular points. To do so, singular point p_z, localized in the intersection between the vertical axis S_z and the surface of the sphere, is studied for the different tensors in the schematic classification (Figs. 5 and 8). Near p_z the surface of the sphere can be approximated by the horizontal plane H, tangent to the sphere at p_z (Fig. 9).

The co-ordinates on the horizontal plane H, of a point p of the surface of the sphere, close to p_z, can be calculated from angles Θ and ϕ:

$$\Delta x = \Delta\Theta \cos(\phi), \quad \Delta y = \Delta\Theta \sin(\phi), \tag{18}$$

where symbol Δ indicates that the size of variables is small. Using equation (8), F_n can be expressed close to p_z by replacing $\sin^2(\Delta\Theta)$ and $\cos^2(\Delta\Theta)$ by their series developments, keeping only the terms whose order is less or equal than $\Delta\Theta^2$:

$$F_n = (\lambda_x \cos^2(\phi) + \lambda_y \sin^2(\phi)) \sin^2(\Delta\Theta)$$

$$+ \lambda_z \cos^2(\Delta\Theta) \Rightarrow$$

$$F_n = (\lambda_x \cos^2(\phi) + \lambda_y \sin^2(\phi)) \Delta\Theta^2$$

$$+ \lambda_z (1 - \Delta\Theta^2). \tag{19}$$

Using variables Δx and Δy, it is obtained:

$$F_n - \lambda_z = \Delta\Theta^2 \cos^2(\phi)(\lambda_x - \lambda_z)$$

$$+ \Delta\Theta^2 \sin^2(\phi)(\lambda_y - \lambda_z) \Rightarrow$$

$$1 = \frac{\Delta x^2}{\left[\dfrac{F_n - \lambda_z}{\lambda_x - \lambda_z}\right]} + \frac{\Delta y^2}{\left[\dfrac{F_n - \lambda_z}{\lambda_y - \lambda_z}\right]} = \frac{\Delta x^2}{A} + \frac{\Delta y^2}{B}. \tag{20}$$

This last equation corresponds to a second degree curve or conic (Bougrov & Nikolski 1983), such that the ratio between A and B is constant for every value of F_n:

$$\frac{A}{B} = \frac{\lambda_y - \lambda_z}{\lambda_x - \lambda_z}. \tag{21}$$

This result is not surprising since F_n is defined on the surface of the sphere by a quadratic form (Arnold 1988, Chap. 2, Section 12-4), that can be expressed in tensor notation by $F_n = T_{ij}n_in_j$.

Using the same approximations, integral curves near p_z are calculated from equation (12):

$$\tan(\Theta) = \Delta\Theta = k_1 |\sin(\phi)|^{R_x-1} |\cos(\phi)|^{-R_x},$$

$$k_1 > 0 \Rightarrow$$

$$\Delta\Theta = k_1 \left|\frac{\Delta y}{\Delta\Theta}\right|^{R_x-1} \left|\frac{\Delta x}{\Delta\Theta}\right|^{-R_x}$$

$$= k_1 |\Delta y|^{R_x-1} |\Delta x|^{-R_x} \Delta\Theta \Rightarrow$$

$$\Delta y = \pm k_2 |\Delta x|^{-R_x/(1-R_x)}$$

$$= \pm k_2 |\Delta x|^{(\lambda_x - \lambda_z)/(\lambda_x - \lambda_z)}$$

$$= \pm k_2 |\Delta x|^{A/B}, \quad k_2 > 0. \tag{22}$$

This last equation corresponds to a *power law*, which is perpendicular in every point to the conic curves calculated previously.

Figure 10 illustrates the equipotentials and integral curves near p_z, for the different tensors of the schematic classification. The potential difference between two contiguous equipotentials is constant. Table 1 indicates the values of parameters A and B as a function of eigenvalues λ_1, λ_2 and λ_3, for the different tectonic regimes.

(1) *In extensive regimes*, p_z corresponds to singular point p_1, $F_n > \lambda_1$ near p_z (Fig. 8) and $A \geq B > 0$. Thus, conic curves correspond to ellipses whose long axis is parallel to S_x and whose small axis is parallel to S_y, their half-lengths being $\sqrt{A}$ and $\sqrt{B}$, respectively.

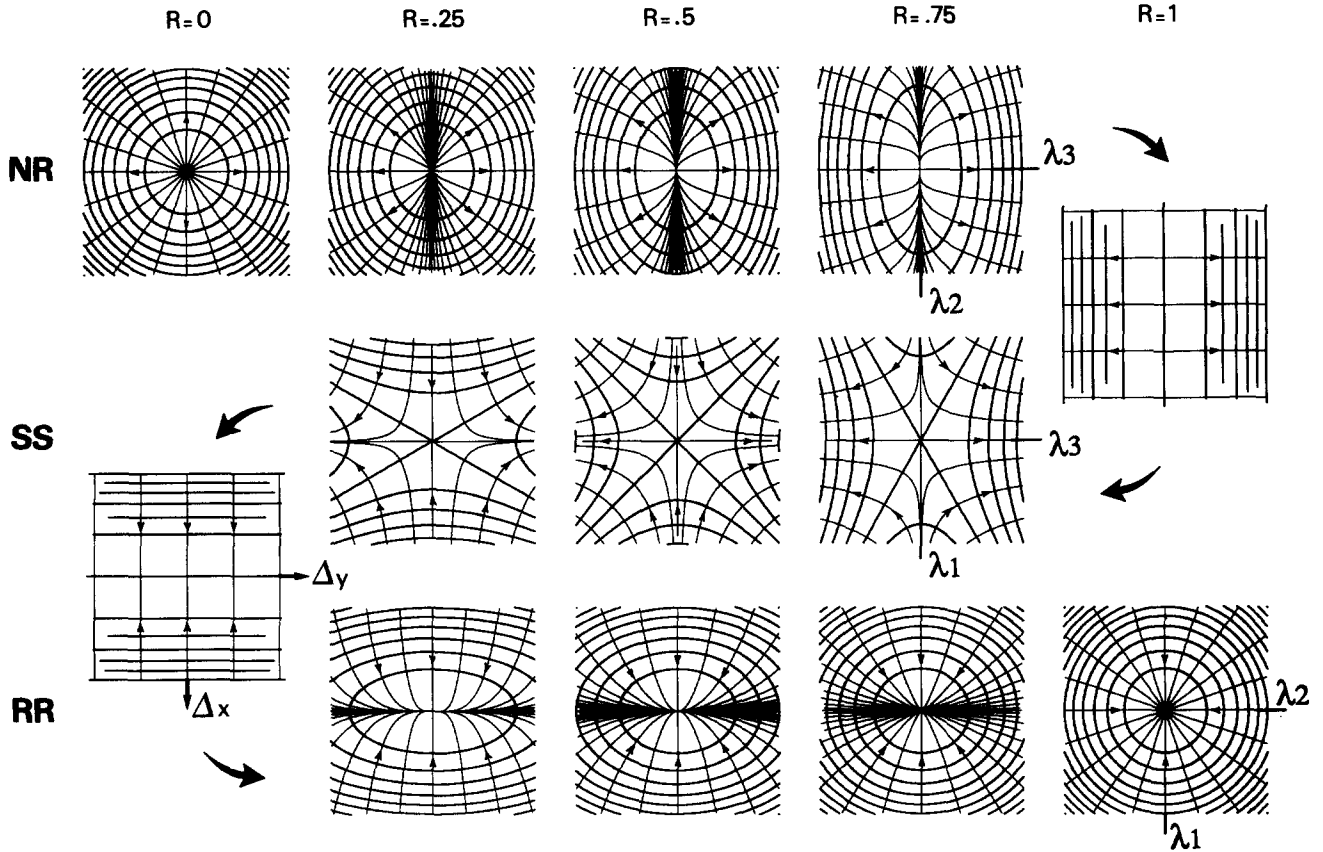R=0   R=.25   R=.5   R=.75   R=1

Fig. 10. Integral curves and equipotentials near singular point p_z, for different tectonic regimes. Notice that p_z corresponds to a diverging node, a saddle point or a converging node, depending on the tectonic regime.

Equation (22) describing integral curves corresponds to a power law whose exponent $A/B \geq 1$. If $\lambda_2 = \lambda_3$, then $A = B$, and consequently the ellipses reduce to circles, and integral curves are straight lines placed radially around p_1. Conversely, when $\lambda_2 \to \lambda_1$, then $A \gg B$, and the ellipses are more and more elongated. In the limiting case where $\lambda_2 = \lambda_1$, the conic corresponds to a couple of straight lines parallel to the S_x axis, and integral curves correspond to straight lines parallel to the S_y axis.

(2) In a strike-slip regime, p_z corresponds to singular point p_2. Three cases are considered depending on the value of F_n near p_z.

(a) If $F_n < \lambda_2$, then $B < 0 < A$, and the conic corresponds to an hyperbola whose focal axis is S_x.

(b) If $F_n > \lambda_2$, then $A < 0 < B$, and the conic corresponds to a hyperbola whose focal axis is S_y.

(c) If $F_n = \lambda_2$, the equation of a couple of convergent

lines whose slope is $\sqrt{-B/A}$, is obtained by multiplying the conic equation (20) by $(F_n - \lambda_2)$:

$$F_n - \lambda_2 = (\lambda_1 - \lambda_2)\,\Delta x^2 + (\lambda_3 - \lambda_2)\,\Delta y^2 = 0 \Rightarrow$$

$$\Delta y^2 = -\left[\frac{\lambda_1 - \lambda_2}{\lambda_3 - \lambda_2}\right]\Delta x^2 = -\left[\frac{B}{A}\right]\Delta x^2. \qquad (23)$$

This pair of straight lines define the asymptotes of the two families of hyperbolas mentioned previously. Notice that if $\lambda_2 \to \lambda_3$, the asymptotes tend to be parallel to the S_y axis, since $\sqrt{-B/A} \to \infty$. In the same way, if $\lambda_2 \to \lambda_1$, the asymptotes tend to be parallel to the S_x axis, since $\sqrt{-B/A} \to 0$. Integral curves near p_2 correspond to a power law whose exponent $A/B < 0$.

(3) In compressive regime, p_z corresponds to singular point p_3. Moreover, $F_n < \lambda_3$ near p_z, and $B \geq A > 0$. The conic curves correspond to ellipses whose long axis is

Table 1. Parameters A and B defining integral curves and equipotentials near p_z, as a function of eigenvalues λ_1, λ_2 and λ_3, for different tectonic regimes.

Regime	p_z	λ_x	λ_y	λ_z	A	B	A/B
Extensive	p_1	λ_2	λ_3	λ_1	$\dfrac{F_n - \lambda_1}{\lambda_2 - \lambda_1}$	$\dfrac{F_n - \lambda_1}{\lambda_3 - \lambda_1}$	$\dfrac{\lambda_3 - \lambda_1}{\lambda_2 - \lambda_1}$
Strike-slip	p_2	λ_1	λ_3	λ_2	$\dfrac{F_n - \lambda_2}{\lambda_1 - \lambda_2}$	$\dfrac{F_n - \lambda_2}{\lambda_3 - \lambda_2}$	$\dfrac{\lambda_3 - \lambda_2}{\lambda_1 - \lambda_2}$
Compressive	p_3	λ_1	λ_2	λ_3	$\dfrac{F_n - \lambda_3}{\lambda_1 - \lambda_3}$	$\dfrac{F_n - \lambda_3}{\lambda_2 - \lambda_3}$	$\dfrac{\lambda_2 - \lambda_3}{\lambda_1 - \lambda_3}$

parallel to S_y and whose short axis is parallel to S_x, their half-lengths being $\sqrt{B}$ and $\sqrt{A}$, respectively. Equation (22) describing integral curves corresponds to a power law whose exponent $0 \leq A/B \leq 1$. If $\lambda_2 = \lambda_1$, then $A = B$, and consequently the ellipses reduce to circles, and integral curves are straight lines placed radially around p_3. Conversely, when $\lambda_2 \to \lambda_3$, then $B \gg A$, and the ellipses are more and more elongated. In the limiting case where $\lambda_2 = \lambda_3$, the conic corresponds to a pair of straight lines parallel to the S_y axis and integral curves correspond to straight lines parallel to the S_x axis.

In the different cases presented in Fig. 10, the distance between two contiguous equipotentials increases as we get closer to the singular point p_z. This means that the magnitude of F_r decreases as we get closer to the singularity, where F_r is zero.

(4) *In an extensive regime*, the half-length of the short axis of the ellipses corresponding to a given equipotential, is constant for different values of the R ratio. Indeed, near p_z, the short axis of the ellipses is tangent to the principal circle κ_{31} (Fig. 6). The magnitude of F_r in any point of κ_{31}, is independent of the shape ratio R (Fig. 8b). The half-length of the long axis of ellipses corresponding to the same equipotential increases as a function of the R ratio because, near p_z, the long axis of the ellipses is tangent to principal circle κ_{12} (Fig. 6). The magnitude of F_r in any point of κ_{12}, is proportional to $(1-R)$ and it decreases when R increases (Fig. 8b). Analogous results can be proposed in *compressive regime*, for equipotentials near p_z.

(5) *In strike-slip regimes*, the equipotentials correspond to hyperbolas. The hyperbolas whose focal axis is Δx, and whose potential difference with respect to p_z is constant, are such that the distance between the vertex of the hyperbola and the origin increases as a function of the R ratio.

In fact, near p_z, the focal axis of these hyperbolas is tangent to principal circle κ_{12} (Fig. 6). Moreover, for each value of the R ratio, the ellipses in extensive regime intersect the Δx axis in the same points as the hyperbolas whose focal axis is Δx.

The hyperbolas whose focal axis is Δy, and whose potential difference with respect to p_z is constant, are such that the distance between the vertex of the hyperbola and the origin decreases as a function of the R ratio.

In this case, the focal axis is tangent to principal circle κ_{23} (Fig. 6) and the magnitude of F_r in a point of κ_{23}, increases proportionally to the value of R (Fig. 8b).

For a fixed value of the R ratio, the hyperbolae whose focal axis is Δy and the ellipses in compressive regime, intersect the Δy axis in the same points.

GRAPHICAL DETERMINATION OF THE STRESS TENSOR SHAPE RATIO FROM FAULT SLIP DATA

One possible application of the theoretical analysis of striations on the sphere consists in estimating stress

parameters from striated microfaults, by identifying each fault plane with its pole on the surface of the sphere (Fig. 2) (i.e. Wallace 1951, Aleksandrowski 1985, Schrader 1991). The striation can be represented by means of a small vector tangent to the surface of the sphere on the pole of the fault plane (Fig. 4a).

In this section a graphical method is presented to estimate the stress tensor shape ratio (i.e. $R = (\sigma_2 - \sigma_3)/(\sigma_1 - \sigma_3)$) from the analysis of striated faults plotted on the surface of the sphere. This method supposes that the stress tensor is homogeneous at the outcrop scale, and that slip direction along a fault plane is parallel to the shear stress (Wallace 1951, Bott 1959, Carey & Brunier 1974).

As explained below, prior to applying this method it is necessary to determine the orientations of the principal stress directions. These orientations can be estimated from other graphical methods (Anderson 1951, Arthaud 1969, McKenzie 1969, Pegoraro 1972, Angelier & Mechler 1977, Etchecopar 1984, Aleksandrowski 1985, Lisle 1987, 1992, Vergely *et al.* 1987, Célérier 1988), or by means of microstructures such as tension gashes and stylolitic peaks (i.e. Arthaud & Mattauer 1969).

Method

To illustrate the principle of the graphical method, in Fig. 11 are plotted on a Wulff stereonet (upper hemisphere), integral curves that are parallel to the applied shear stress for different strike-slip stress tensors (Fig. 7). The orientations of the principal axes in Fig. 11 are fixed, while the stress tensor shape ratio R varies from one stereonet to another. Remember that the orientation of the integral curves at a point m on the stereonet indicates the orientation of the applied shear stress on a fault plane whose unit normal vector passes by m (Figs. 3 and 4a) (this fault plane is tangent to the upper hemisphere at m). For each value of the R ratio are plotted two great circles μ_1 and μ_2 (i.e. two meridians) which correspond to the equipotentials that intersect σ_2 (i.e. λ_2, Fig. 8). The angle ϕ between these great circles and principal axis σ_1 is given by equation (17). Strike-slip reverse domains have been shaded on the stereonets and in the Mohr circle diagrams.

The graphical method to calculate the shape ratio consists of reconstructing integral curves by plotting fault slip data on the surface of the sphere. If the principal directions are known (i.e. by means of other graphical methods), then it is possible to estimate the parameter R by drawing manually great circles μ_1 and μ_2. This procedure is illustrated by means of a theoretical example.

Assume that a striated fault plane population corresponding to a single tectonic phase has been measured. In Fig. 12(a) the striated faults are plotted on a Wulff stereonet (lower hemisphere). Arrows indicate slip direction of the hangingwall with respect to the footwall.

The determination of the stress tensor shape ratio is subdivided into several steps. Each step is illustrated for the whole fault set as follows.
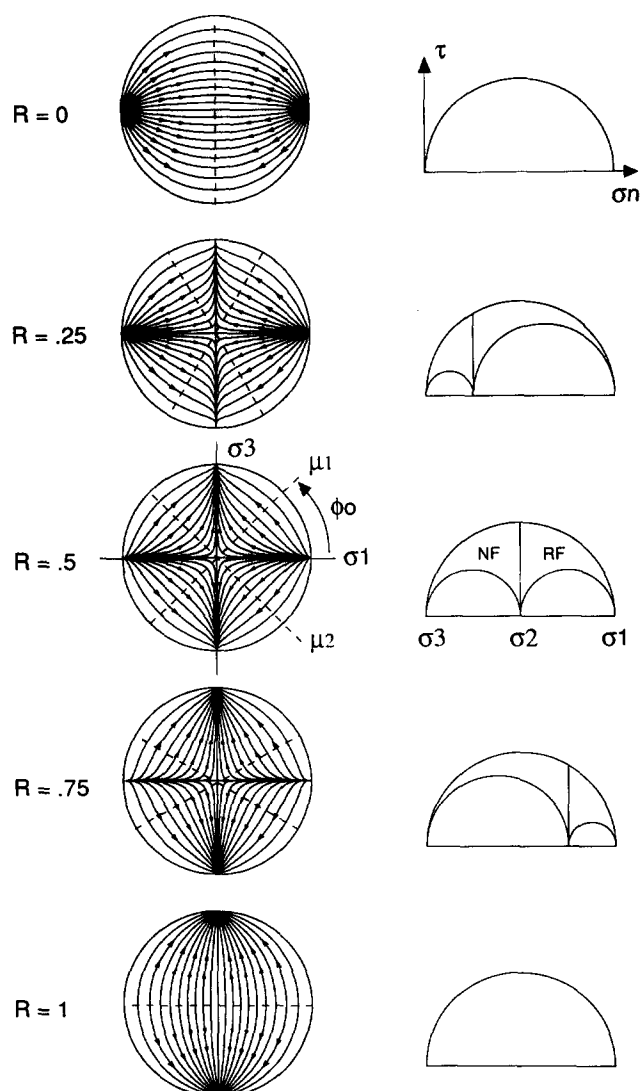
Fig. 11. Wulff projection (upper hemisphere) of integral curves and Mohr diagrams for different stress tensors in strike-slip regime. Curve orientation at any points is parallel to the applied shear stress on a plane that is locally tangent to the hemisphere. RF = reverse faulting (shaded regions); NF = normal faulting.

(1) The orientation of the principal stress directions is estimated by means of another graphical method (e.g. the right-dihedra method), or from microstructures.

(2) Fault planes and their corresponding slip vectors are rotated such that the intermediate axis σ_2 becomes vertical (Fig. 12b).

(3) The pole of each fault plane is then plotted on the stereonet (*upper hemisphere*) (Fig. 12c). A vector indicating the local slip direction on the tangent plane is plotted from each pole. The angle between the strike of the tangent plane and the slip vector in the stereonet is equal to the rake α of the striated fault (Figs. 13a & b) (this results from the angle-preserving property of the Wulff projection).

(4) Curves that are locally tangent to the slip vectors are reconstructed manually (Fig. 12c) (they should be well defined if enough fault data are available). These curves are identified with the integral curves presented by supposing that slip direction is parallel to the applied shear stress.

(5) Two symmetrical lines corresponding to great circles μ_1 and μ_2 are drawn manually. These lines should intersect integral curves perpendicularly.

(6) The angle ϕ_o between the great circle μ_1 or μ_2 and the horizontal axis σ_1, allows to estimate graphically the shape ratio R by means of the function plotted in Fig. 13(d) which corresponds to equation (17).

In this particular example $\phi_o = \pi/4$ and the stress shape ratio $R = 0.5$.

Note that when fault plane poles are localized in principal circle (σ_1, σ_3) (i.e. fault planes are vertical in strike-slip reference frame), it is not possible to determine the shape ratio R. In fact, the shear stress orientation is independent of the shape ratio in principal circle (σ_1, σ_3) (Figs. 7 and 11). Fault plane poles are frequently located in this principal circle when fresh failures occur within intact rocks (Anderson 1951).

This method allows the identification of fault planes that are not compatible with the stress tensor solution. A simple criteria is to test whether the fault slip vector is oblique or tangent to the integral curves constructed from the remaining faults.

It is also possible to determine graphically the interval of potential fault slip orientation corresponding to shape ratios R between 0 and 1 (Fig. 13c) (Wallace 1951, Lisle 1987). For $R = 0$ and $R = 1$, the fault slip vector (plotted from the pole) is tangent to principal circles around σ_1 and σ_3, respectively. If slip orientation is not in the interval determined graphically, fault movement is not compatible with the orientation of the stress axes.

CONCLUSIONS

The orientation of striations on the surface of a rigid spherical body linked to a symmetrical tensor (which can represent either the stress tensor around the sphere or the displacement tensor between the pebble and the matrix), depends on four parameters: the orientation of the principal axes and a ratio that characterizes the form of the ellipsoid.

Thus, the analysis of a single striated pebble in terms of stress permits the estimation of the local value of these parameters in the conglomerate. The interpretation of striated pebbles in terms of strain provides a method for estimating three-dimensional strain parameters, suitable when deformations are small.

It has been supposed that the stress or displacement tensor is homogeneous around the sphere. This hypothesis should hold if deformations are small and if pebbles in the conglomerate are not too closely packed. If pebbles are close together, stress concentrations might be expected at contact points between pebbles (i.e. near singular points) (McEwen 1981).

Calculated integral curves that are parallel to striations at every point, and equipotentials that are perpendicular to the integral curves, are well suited to describe the topology of the striation vector field on the sphere (i.e. size and orientation of striations in terms of strain). The interpretation of these curves in terms of
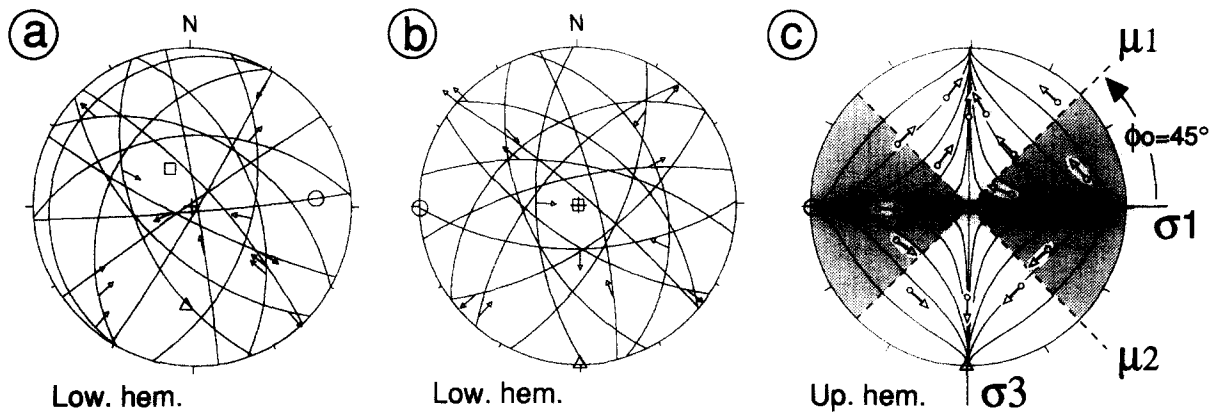
Fig. 12. Wulff projection of fault planes, striation vectors and principal stress axes (σ_1 = circle, σ_2 = square, σ_3 = triangle). Arrows indicate movement of hangingwall with respect to footwall. Low. hem. = lower hemisphere; Up. hem. = upper hemisphere. (a) Theoretical data. (b) Data are rotated so that σ_2 becomes vertical and σ_1 is oriented E–W. (c) Striation vectors are plotted on the poles of the planes (see Figs. 13a & b). Dashed lines separate reverse faulting (shaded region) from normal faulting. Notice that arrows are locally tangent to integral curves.
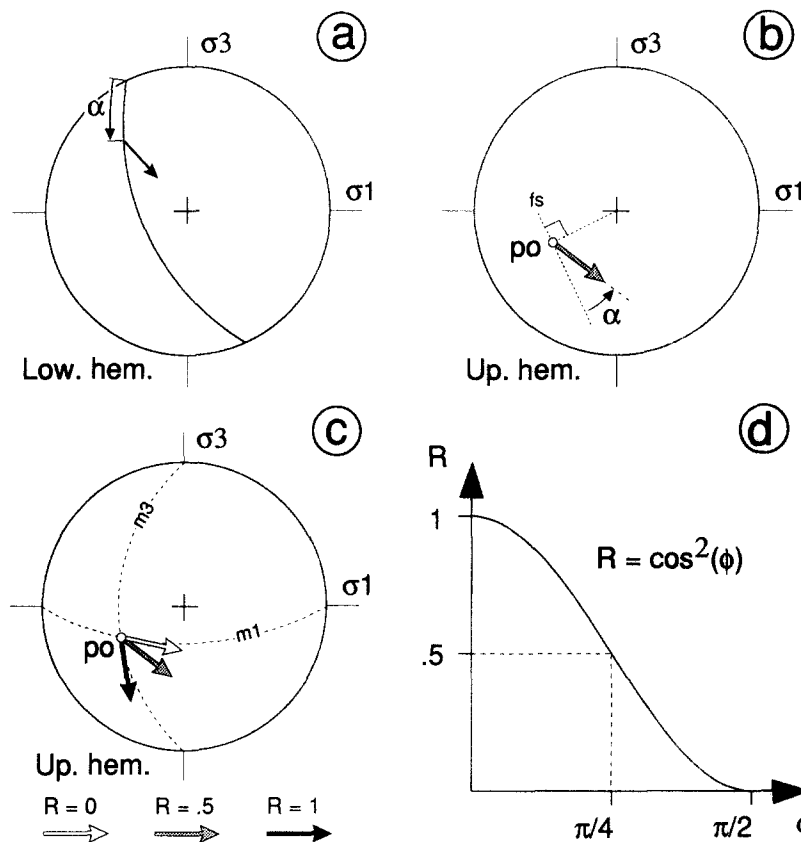

Fig. 13. (a) Wulff projection (lower hemisphere) of a fault plane and its striation vector. α = rake of the striation measured on the fault plane. (b) Construction of the slip vector on the pole of the plane in a Wulff projection (upper hemisphere). po = pole of the fault plane; fs = dotted line parallel to the fault strike. The orientation of the slip vector on the pole indicates movement on the plane that is tangent to the hemisphere at po. (c) Slip vectors on the pole for different values of stress tensor shape ratio R. m1 = great circle around σ_1 axis, passing by the pole; m3 = great circle around σ_3 axis, passing by the pole. (d) Plot of the function defining the relation between the angle ϕ_0 (Figs. 11 and 12) and the stress tensor shape ratio R (equation 17). This curve allows to estimate graphically the parameter R from the value of ϕ_0.

stress is useful for analysing the kinematics of faulting as a function of the stress regime and of fault plane orientation: the magnitude and the orientation of the shear and normal stress vectors are easily visualized by means of integral curves and equipotentials.

The analysis of integral curves and equipotentials close to singular points allows determination of the

orientation of the striations as a function of the tensor shape ratio, in these unstable zones. This analysis shows that the information available from the striation pattern close to any singular point is sufficient to characterize the three-dimensional stress or coaxial strain regime.

The application of this theory to the analysis of fault slip data makes it possible to estimate graphically the

stress shape ratio, once the principal stress directions have been determined (i.e. by means of other graphical methods).

REFERENCES

Aleksandrowski, P. 1985. Graphical determination of principal stress directions for slickenside lineation populations: an attempt to modify Arthaud's method. *J. Struct. Geol.* **7**, 73–82.

Anderson, E. M. 1951. The Dynamics of Faulting. Oliver & Boyd, Edinburgh.

Angelier, J. 1979. Determination of the mean principal stresses for a given fault population. *Tectonophysics* **56**, 17–26.

Angelier, J. 1990. Inversion of field data in fault tectonics to obtain the regional stress—III. A new rapid direct inversion method by analytical means. *Geophys. J. Int.* **103**, 363–376.

Angelier, J. & Mechler, P. 1977. Sur une méthode graphique de recherche des contraintes principales également utilisable en tectonique et en seismologie: la méthode des dièdres droits. *Bull. Soc. géol. Fr.* **19**, 1309–1318.

Armijo, R. & Cisternas, A. 1978. Un probléme inverse en microtectonique cassante. *C. r. Acad. Sci., Paris* **287**, 595–598.

Arnold, V. 1988. *Equations Différentielles Ordinaires.* Mir, Moscou.

Arthaud, F. 1969. Méthode de détermination graphique des directions de raccourcissement, d'allongement et intermédiaire d'une population de failles. *Bull. Soc. géol. Fr.* **11**, 729–737.

Arthaud, F. & Mattauer, M. 1969. Exemples de stylolites d'origine tectonique dans le Languedoc, leurs relations avec la tectonique cassante. *Bull. Soc. géol. Fr.* **7**, 738–744.

Bott, M. H. P. 1959. The mechanics of oblique slip faulting. *Geol. Mag.* **96**, 109–117.

Bougrov, Y. & Nikolski, S. 1983. *Cours de Mathématiques Supérieures. Tome I.* Mir, Moscou.

Campredon, R., Franco, M., Giannerini, G., Gigot, P., Irr, F., Lanteaume, M., Spini, H. & Tapoul, J. F. 1977. Les déformations de conglomérats pliocènes de l'Arc de Nice (Chaînes subalpines méridionales). *C. r. Somm. Soc. géol. Fr.* **2**, 75–77.

Carey, E. 1979. Recherche des directions principales de contraintes associées au jeu d'une population de failles. *Rev. Géol. dyn. Géogr. phys., Paris* **21**, 57–66.

Carey, E. & Brunier, B. 1974. Analyse théorique et numérique d'un modèle mécanique élémentaire appliqué à l'étude d'une population de failles. *C. r. Acad. Sci., Paris* **D179**, 891–894.

Casagrande Fioretti, L. 1985. Evolution tectonosédimentaire post-Eocène de la bordure ouest des Baronnies et du Massif de Suzette. (Chaînes subalpines des Baronnies). Unpublished Thèse de Doctorat, Université de Paris-Sud.

Célérier, B. 1988. How much does slip on a reactivated fault plane constrain the stress tensor? *Tectonics* **7**, 1257–1278.

Combes, P. 1984. La tectonique récente de la provence occidentale. Microtectonique, caractéristiques dynamiques et cinématiques. Méthodologie de zonation tectonique et relations avec la séismicité. Unpublished thèse de doctorat, Université Louis Pasteur de Strasbourg, France.

De Paor, D. G. 1983. Orthographic analysis of geological structures—I. Deformation theory. *J. Struct. Geol.* **5**, 255–277.

Eidelman, A. & Reches, Z. 1992. Fractured pebbles—a new stress indicator. *Geology* **20**, 307–310.

Estevez, A., Lopez-Garrido, A. C. & Sanz de Galdeano, C. 1976. Estudio de las deformaciones recientes en el sector del Negrantín (depresión de Guadix-Baza). Reunión sobre la geodinámica de la Cordillera Bética y mar de Alborán, sección de geológicas, Facultad de Ciencias, Universidad de Granada.

Etchecopar, A. 1984. Etude des états de contrainte en tectonique cassante et simulation de déformations plastiques (approche mathématique). Unpublished thèse d'Etat, Universite de Montpellier II. France.

Etchecopar, A. & Malavieille, J. 1987. Computer models of pressure shadows: a method for strain measurement and shear-sense determination. *J. Struct. Geol.* **9**, 667–677.

Etchecopar, A., Vasseur, G. & Diagnières, M. 1981. An inverse problem in microtectonics for the determination of stress tensors from fault striation analysis. *J. Struct. Geol.* **3**, 51–65.

Fleischmann, K. & Nemcok, M. 1991. Paleostress inversion of fault-slip data using the shear stress solution of Means (1989). *Tectonophysics* **196**, 195–202.

Galindo-Zaldivar, J. & Gonzalez-Lodeiro, F. 1988. Faulting phase differentiation by means of computer search on a grid pattern. *Annales Tectonicæ* **II**, 90–97.

Gephart, J. W. & Forsyth, D. W. 1984. An improved method for determing the regional stress tensor using earthquake focal mechanism data: an application to the San Fernando earthquake sequence. *J. geophys. Res.* **89**, 9305–9320.

Germain, P. 1986. *Mécanique, Tome I.* Ecole Polytechnique, Ellipses, Palaiseau, France.

Guiraud, M., Laborde, O. & Philip, H. 1989. Characterization of various types of deformation and their corresponding deviatoric stress tensors using microfault analysis. *Tectonophysics* **170**, 289–316.

Hoeppener, R., Brix, M. & Vollbrecht, A. 1983. Some aspects on the origin of fold-type fabrics—theory, experiments and field applications. *Geol. Rdsch.* **72**, 421–450.

Lisle, R. J. 1987. Principal stress orientations from faults: an additional constraint. *Annales Tectonicæ* **2**, 155–158.

Lisle, R. J. 1992. New method of estimating regional stress orientations: application to focal mechanism data of recent British earthquakes. *Geophys. J. Int.* **110**, 276–282.

McEwen, T. J. 1981. Brittle deformation in pitted pebble conglomerates. *J. Struct. Geol.* **3**, 25–37.

McKenzie, D. P. 1969. The relation between fault plane solutions for earthquakes and the directions of principal stresses. *Bull. seism. Soc. Am.* **59**, 591–601.

Michael, A. 1984. Determination of stress from slip data: faults and folds. *J. geophys. Res.* **89**, 11,517–11,526.

Munkres, J. R. 1991. *Analysis on Manifolds.* Addison-Wesley, Redwood City.

Pegoraro, O. 1972. Application de la microtectonique à une étude de néotectonique sur le golfe maliaque (Grèce centrale). Unpublished thèse 3eme cycle tectonophysique, Montpellier.

Petit, J. P., Raynaud, S. & Cautru, J. P. 1985. Microtectonique cassante lors du plissement d'un conglomérat (Mio-Pliocène du Haut Atlas—Maroc). *Bull. Soc. géol. Fr.* **3**, 415–421.

Philip, H. 1987. Plio-Quaternary evolution of the stress field in Mediterranean zones of subduction and collision. *Annales Geophysicæ* **5B**, 301–320.

Reches, Z. 1987. Determination of the tectonic stress tensor from slip along faults that obey the Coulomb yield condition. *Tectonics* **6**, 849–861.

Ritz, J. F. 1991. Evolution du champ de contraintes dans les Alpes du Sud depuis la fin de l'Oligocène. Implications sismotectoniques. Unpublished thèse de doctorat, Université de Montpellier II, France.

Rivera, L. & Cisternas, A. 1990. Stress tensor and fault plane solutions for a population of earthquakes. *Bull. seism. Soc. Am.* **80**, 600–614.

Sassi, W. & Carey-Gailhardis, E. 1987. Interprétation mécanique du glissement sur les failles: introduction d'un critère de frottement. *Annales Tectonicæ* **I**, 139–154.

Schrader, F. 1988. Symmetry of pebble-deformation involving solution pits and slip-lineations in the northern Alpine Molasse Basin. *J. Struct. Geol.* **10**, 41–52.

Schrader, F. 1991. Field-based analysis of faults, stylolites and extension gashes. *Annales Tectonicæ* **2**, 91–101.

Séranne, M. 1988. Tectonique des bassins dévoniens de Norvège: mise en évidence de bassins sédimentaires en extension formés par amincissement d'une croûte orogénique épaissie. Unpublished thèse de Doctorat, Université de Montpellier II, France.

Séranne, M. & Séguret, M. 1987. The Devonian basins of western Norway: tectonics and kinematics of an extending crust. In: *Continental Extensional Tectonics* (edited by Coward, M. P., Dewey, J. F. & Hancock, P. L.). *Spec. Publs geol. Soc. Lond.* **28**, 537–548.

Spiegel, M. R. 1987. *Analyse Vectorielle.* Série Schaum, McGraw-Hill, New York.

Tajima F. & Célérier B. 1989. Possible focal mechanism change during

reactivation of a previously ruptured subduction zone and stress tensor implications. *Geophys. J. Int.* **98**, 301–316.

Twiss, R. J., Protzman, G. M. & Hurst, S. D. 1991. Theory of slickenline patterns based on the velocity gradient tensor and microrotation. *Tectonophysics* **186**, 215–239.

Vergely, P., Sassi, W. & Carey-Gailhardis, E. 1987. Analyse graphique des failles à l'aide des focalisations de stries. *Bull. Soc. géol. Fr.* **2**, 395–402.

Wallace, R. E. 1951. Geometry of shearing stress and relation to faulting. *J. Geol.* **59**, 118–130.

Will, Th. & Powell, R. 1991. A robust approach to the calculation of paleostress fields from fault plane data. *J. Struct. Geol.* **13**, 813–821.

APPENDIX A

In this Appendix integral equation (11) in the text is solved to obtain an analytical formula for integral curves on the surface of the sphere. Equation (11) is given by:

$$\int \frac{d\Theta}{\cos(\Theta)\sin(\Theta)} = \int \left[\frac{R_x}{\cos(\phi)\sin(\phi)} - \frac{\cos(\phi)}{\sin(\phi)} \right] d\phi. \quad (A1)$$

To evaluate this integral the following primitives are calculated:

(a) $\int \dfrac{\cos(\beta)}{\sin(\beta)} d\beta \Rightarrow$ by substituting

$$u = \sin(\beta), \; du = \cos(\beta) \, d\beta \Rightarrow$$

$$\int \frac{\cos(\beta)}{\sin(\beta)} d\beta = \int \frac{du}{u} = \ln|u| + k = \ln|\sin(\beta)| + k,$$

$$\beta \neq n\pi. \quad (A2)$$

(b) $\int \dfrac{d\beta}{\cos(\beta)\sin(\beta)} \Rightarrow$ by substituting

$$u = \tan(\beta), \sin(2\beta) = \frac{2u}{1+u^2},$$

$$d\beta = \frac{du}{1+u^2} \Rightarrow$$

$$\int \frac{d\beta}{\cos(\beta)\sin(\beta)} = 2 \int \frac{d\beta}{\sin(2\beta)} = \int \frac{du}{u}$$

$$= \ln|u| + k = \ln|\tan(\beta)| + k,$$

$$\beta \neq \pi/2 + n\pi. \quad (A3)$$

Replacing these expressions in the integral equation gives:

$$\ln|\tan(\Theta)| = R_x \ln|\tan(\phi)| - \ln|\sin(\phi)| + k$$

$$= \ln\left[\frac{k_1|\tan(\phi)|^{R_x}}{|\sin(\phi)|} \right], \quad k_1 > 0,$$

$$\Rightarrow \tan(\Theta) = \pm k_1 |\sin(\phi)|^{R_x-1} |\cos(\phi)|^{-R_x}$$

$$= \pm k_1 |\sin(\phi)|^{(\lambda_x-\lambda_z)/(\lambda_y-\lambda_x)}$$

$$\times |\cos(\phi)|^{(\lambda_z-\lambda_y)/(\lambda_y-\lambda_x)} = \zeta(\phi), \quad \phi \neq n\pi/2,$$

$$\Rightarrow \Theta = \text{arctg}(\zeta(\phi)) = \varphi(\phi), \quad (A4)$$

where the function $\varphi(\phi)$ defines integral curves on the surface of the sphere.

This equation can be checked by showing that (Arnold 1988, Chap. 1, Section 1-4):

$$\frac{1}{\sin(\Theta)} \frac{d\varphi(\phi)}{d\phi} = v(\Theta, \phi) \Rightarrow \frac{1}{\sin(\varphi(\phi))} \frac{d\varphi(\phi)}{d\phi} = v(\phi(\phi), \phi), \quad (A5)$$

where $v(\Theta, \phi)$ is defined by equation (9) in the text.

APPENDIX B

In this Appendix equation (13) in the text is proved, which states that

$$\mathbf{F}_r = \frac{1}{2} \nabla_S |\mathbf{F}_n|, \quad (B1)$$

where ∇_S is the gradient operator limited to the surface of the sphere.

This formula can be evaluated by calculating the gradient on the surface of the unit sphere, of the potential function $[(1/2)|\mathbf{F}_n|]$. This function can be expressed in spherical co-ordinates by means of equation (8) in the text:

$$\frac{1}{2}|\mathbf{F}_n| = \frac{1}{2}F'_{c\rho}$$

$$= \frac{1}{2}[(\lambda_x \cos^2(\phi) + \lambda_y \sin^2(\phi)) \sin^2(\Theta) + \lambda_z \cos^2(\Theta)]. \quad (B2)$$

The two components of the gradient that are tangent to the surface of the sphere are given by:

$$\frac{1}{2}\nabla_S|\mathbf{F}_n| = \frac{1}{2}\left[\frac{\partial F'_{c\rho}}{\rho \partial\Theta} \mathbf{e}\Theta + \frac{\partial F'_{c\rho}}{\rho\sin(\Theta)\partial\phi} \mathbf{e}\phi \right], \quad (B3)$$

where $\rho = 1$.

It can easily be shown that:

$$\frac{\partial F'_{c\rho}}{2\rho\partial\Theta} = \sin(\Theta)\cos(\Theta)(\lambda_x \cos^2(\phi)$$

$$+ \lambda_y \sin^2(\phi) - \lambda_z) = F'_{e\Theta} \quad (B4)$$

$$\frac{\partial F'_{c\rho}}{2\rho\sin(\Theta)\partial\phi} = (\lambda_y - \lambda_x)\sin(\Theta)\cos(\phi)\sin(\phi) = F'_{e\phi}, \quad (B5)$$

where $F'_{e\Theta}$ and $F'_{e\phi}$ are the components of $\mathbf{F}_r$ in directions $\mathbf{e}\Theta$ and $\mathbf{e}\phi$, respectively (equation 8 in the text).